Measurement of the neutron charge radius

A Letter of Intent submitted to PAC 48

H. Atac, M. Paolone, N. Sparveris[1]
Temple University, Philadelphia, PA 19122, USA

Z.E. Meziani
Argonne National Laboratory, Lemont, IL 60439, USA

A. Camsonne, M. Jones
Thomas Jefferson National Accelerator Facility, Newport News, VA, USA

[1]contact:sparveri@temple.edu

Abstract

The neutron is a cornerstone in our depiction of the visible universe, and the precise measurement of its charge radius, r_n, is among the most essential parts of unraveling its structure. Despite the neutrons net zero electric charge, the asymmetric distribution of the positively-charged (up) and negatively-charged (down) quarks in the system lead to a negative r_n^2. The determination of r_n has historically relied exclusively on measurements of the neutron-electron scattering length, b_{ne}, from neutron scattering off electrons bound in diamagnetic atoms. The r_n measurements accepted by the particle data group are now over two decades old and have long exhibited unresolved discrepancies. Here we propose a new r_n measurement, based on a novel extraction of the neutron electric form factor, G_E^n, at low four-momentum transfer squared (Q^2) from measurements of the $N \to \Delta$ transition, by exploiting the long known connection between the quadrupole transitions and the neutron electric form factor. The proposed measurements will access $\langle r_n^2 \rangle$ with a ± 0.005 (fm^2) uncertainty, and will offer new input toward addressing the long standing discrepancies in r_n measurements. Furthermore, the measurements will test an electric form factor based charge-radius extraction methodology on the isospin partner of the proton, whose corresponding charge radius measurements have been questioned recently in light of the proton radius puzzle. New data will also allow the flavor decomposition of the nucleon electromagnetic form factors at low momentum transfers, and from the derivative of the flavor dependent Dirac form factors at $Q^2 = 0$ the mean square radii of the quark distributions will be determined.

1 Introduction

The study of the nucleon charge radius has been historically instrumental towards the understanding of the nucleon structure. Employing different techniques in extracting this fundamental quantity has proven most valuable, as recently exhibited in the case of the proton. The recent disagreement of the proton charge radius, r_p, as determined using the measurement of the Lamb shift in the muonic hydrogen atom[1], with the earlier results based on the hydrogen atom and the electron scattering measurement, gave rise to the proton radius puzzle[2]. This, in turn, led to a significant reassessment of the methods and analyses utilized in the radius extraction, and to the consideration of physics beyond the standard model as potential solutions to resolve this discrepancy. Many atomic and nuclear physics techniques have been applied to extract the proton r_p, while for the neutron, isospin partner of the proton, the r_n determination is more challenging since no equivalent atomic method is possible and the electron scattering method suffers from severe limitations due to the absence of a free neutron target. Contrary to the proton, the extraction of r_n has been uniquely based on the measurement of the *neutron*-electron scattering length b_{ne}, where low-energy neutrons are scattered by electrons bound in diamagnetic atoms. The $\langle r_n^2 \rangle$ measurements adopted by PDG[3–6], the most recent of which is dated two decades ago, exhibit discrepancies, with the values ranging from $\langle r_n^2 \rangle = -0.115 \pm 0.002 \pm 0.003$ (fm^2)[3] to $\langle r_n^2 \rangle = -0.134 \pm 0.009$ (fm^2)[5]. Among the plausible explanations that have been suggested for this, one can find the effect of resonance corrections and of the electric polarizability, as discussed e.g. in[4], but these discrepancies have not been fully resolved.

An alternative way to determine r_n is offered by measuring the slope of the neutron electric form factor, G_E^n, at $Q^2 \to 0$, which is proportional to $\langle r_n^2 \rangle$. In the past, determinations of G_E^n at finite Q^2 were typically carried out by measuring double polarization observables in quasi-elastic electron scattering from polarized deuterium or ^{3}He targets using polarized electron beams[7–20]. However, these measurements were not able to access G_E^n at a sufficiently low Q^2 range for the slope, and subsequently the $\langle r_n^2 \rangle$, to be determined. Here we propose to follow an alternative path to access G_E^n. It has long been known[21,22] that the ratios of the quadrupole to the magnetic dipole transition form factors of the proton, $C2/M1$ and $E2/M1$, are related to the neutron elastic form factors ratio G_E^n/G_M^n. The transition form factors can be measured with high precision at low momentum transfers, as recent experiments have shown[23–27]. This, in-turn, opens up the path to access the G_E^n at low momentum transfers from high precision measurements of the quadrupole transition form factors, and from the G_E^n slope at $Q^2 = 0$ to determine the neutron charge radius r_n.

2 Measurement of G_E^n

A consequence of the SU(6) spin and flavor symmetry group in which the nucleon and the Δ resonance belong leads to the following expression[21]

$$\frac{G_E^n(Q^2)}{G_M^n(Q^2)} = \frac{Q}{|q|}\frac{2Q}{M_N}\frac{1}{n_b(Q^2)}\frac{C2}{M1}(Q^2) \tag{1}$$

where q is the virtual photon three-momentum transfer magnitude in the γN center of mass frame, M_N is the nucleon mass, and n_b describes three-quark current terms that slightly increase the C2/M1 ratio (or correspondingly decrease the G_E^n/G_M^n), an SU(6) symmetry breaking correction that has been theoretically quantified to $\approx 10\%$[21] (i.e. $n_b \approx 1.1$). If one follows the most conservative path, a theoretical uncertainty can be assigned that is equal to the full magnitude of the symmetry breaking contributions i.e. $n_b = 1.1 \pm 0.1$. Considering the confidence with which the underlying theory is able to determine the level of the symmetry breaking contributions, the above assumption leads to a safe estimation, and most likely to an overestimation, of the theoretical uncertainty.

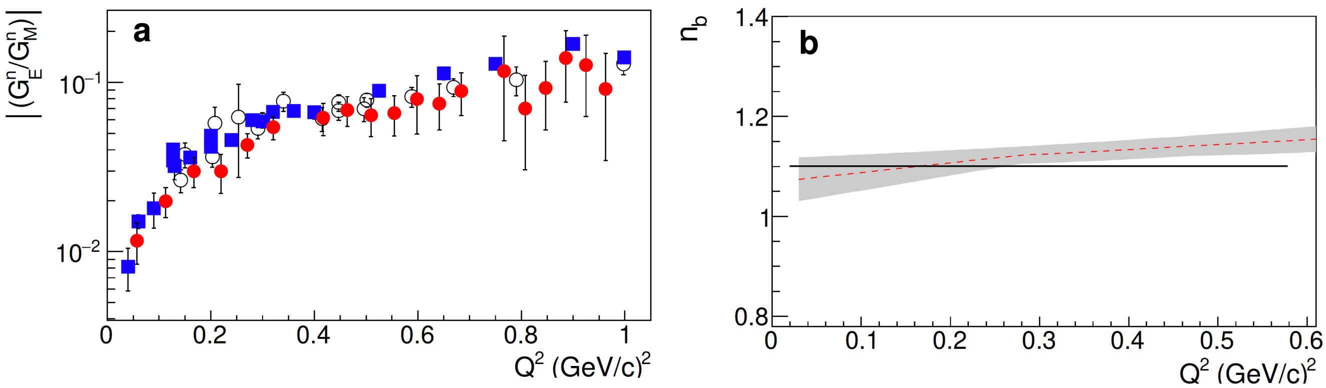

Figure 1. **a)** The G_E^n/G_M^n: neutron world data[7–20] (open-circles), ratios calculated from the $N \to \Delta$ measurements[23–31] through Eq. 1 for $n_b = 1$ (filled-squares), and LQCD results (filled-circles)[32].
b) The breaking corrections n_b (dashed line) and δn_b uncertainty (shaded band) as determined by the experimental data in panel (a). The solid line indicates the theoretical determination of n_b[21].

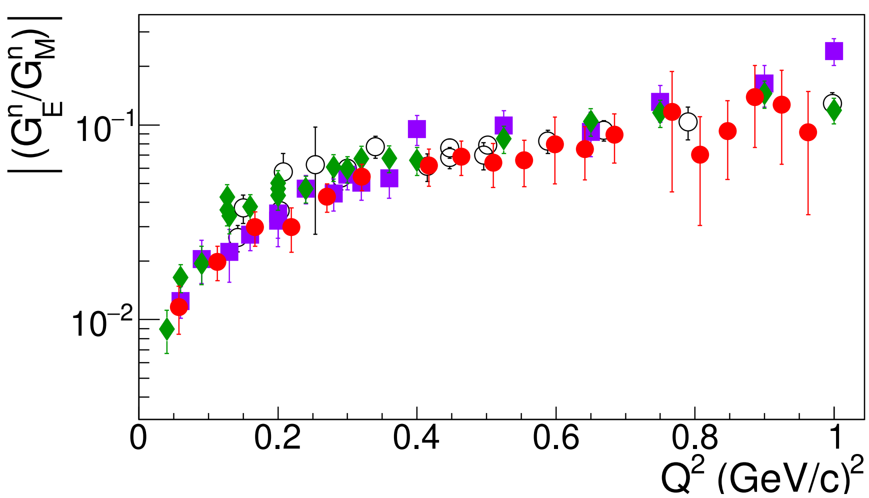

Figure 2. The G_E^n/G_M^n results from the large-N_c analysis with the Coulomb quadrupole data (filled diamonds) and with the Electric quadrupole data (filled boxes) from the experiments[23–31]. The neutron world data (open-circles) and the LQCD results (filled-circles)[32] are the same as in Fig 1.

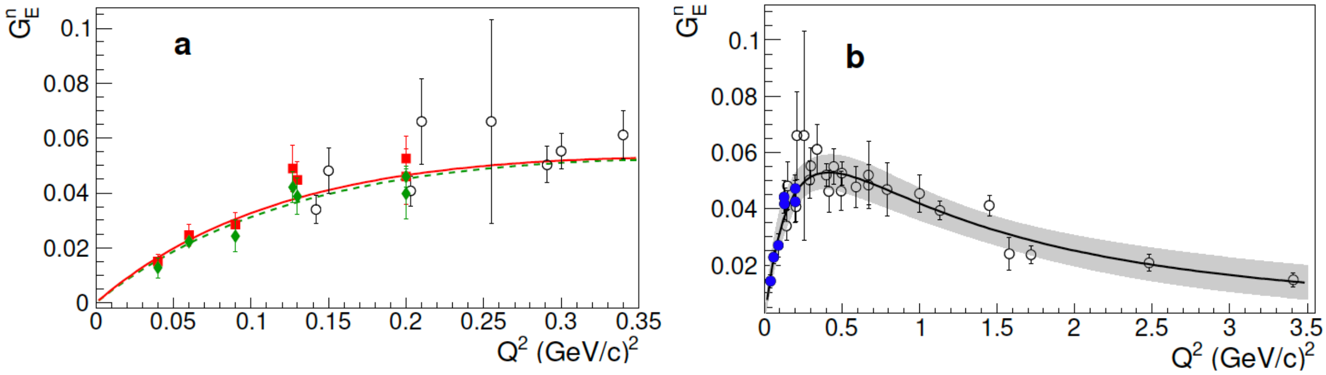

Figure 3. **a)** Green diamonds: the G^n_E results from the SU(6)[21] analysis of the measurements[23–27]. Red boxes: the G^n_E results from the Large-N_c[22] analysis of the data. The fit to the data from the parametrization of Eq. 6 is shown with the dashed and the solid curves, respectively.
b) Blue circles: The final G^n_E results extracted from the weighted average result of the SU(6) and the large-N_c analysis of the[23–27] measurements. The variance of the two data sets is quantified as a theoretical uncertainty. The solid curve shows the fit to the data from the parametrization of Eq. 6, with its uncertainty (shaded band). The G^n_E world data (open-circles)[7–20] are also shown.

The wealth of the $C2/M1$[23–31] and of the G^n_E/G^n_M[7–20] world data allow to go one step further and determine the magnitude of the symmetry breaking corrections. In Fig. 1a we compare the neutron G^n_E/G^n_M world data[7–20] to the G^n_E/G^n_M ratios that have been derived from the $C2/M1$ measurements[23–31] through Eq. 1 with $n_b = 1$, i.e. uncorrected for the symmetry breaking contributions. The $n_b(Q^2)$ can be determined experimentally by parametrizing the two data sets, $F_R(Q^2)$ and $F^*_R(Q^2)$ respectively, and forming their ratio $n_b(Q^2) = F^*_R(Q^2)/F_R(Q^2)$. A variety of functional forms have been explored to identify those that can provide a good fit to the data, and all the appropriate functions are considered in the determination of n_b. The experimentally determined $n_b(Q^2)$ is shown in Fig. 1b. In order to further refine this procedure, at low momentum transfers where neutron data do not exist, we have extracted the ratio G^n_E/G^n_M from numerical simulations within lattice Quantum Chromodynamics (LQCD) using the G^n_E and G^n_M data of Ref[32]. The LQCD data provide input on the Q^2-dependence of the G^n_E/G^n_M ratio based on ab-initio QCD calculations, they allow for further improvements to the parametrization of the neutron data, and lead to a rather small refinement of ≤ 0.003 in the n_b determination.

The LQCD results exhibit a remarkable agreement with the experimental world data, as shown in Fig. 1a. The parameters of the LQCD calculation are such that they reproduce the physical value of the pion mass. Thus, such a calculation eliminates a major source of systematic uncertainties, that is, the need of a chiral extrapolation. Furthermore the lattice results include both the connected and disconnected diagram, and therefore G^n_E and G^n_M include both valence and sea quark contributions.

The experimentally determined $n_b(Q^2)$ is in excellent agreement with the theoretical prediction[21], as seen in Fig. 1b, and this fact offers further credence to the theoretical effort in the literature[21]. Furthermore, it allows to constrain the $n_b(Q^2)$ uncertainty by a factor of two compared to the most conservative $n_b = 1.1 \pm 0.1$, as indicated by the width of the uncertainty band in Fig. 1b. For the analysis of the proposed (projected) measurements, as well as that of the existing data[23–27] at low-Q^2, we have explored the G^n_E extraction under both scenarios i.e. with $n_b = 1.1 \pm 0.1$, and with the n_b as determined from the experimental data (Fig. 1b). The two sets of results come to a remarkable agreement, within a $\leq 3\%$ level (much smaller compared to the overall G^n_E uncertainty), a consequence of the excellent n_b agreement between the two cases. A slightly smaller G_E^n uncertainty is obtained in the latter case due to a smaller level of the n_b uncertainty, which in-turn naturally leads to a slightly improved r_n-uncertainty; nevertheless as this uncertainty is not a leading factor in the r_n extraction the difference in the final result is very small.

The G_E^n uncertainty arises from the following factors:

1. Experimental (statistical and systematic) uncertainties in the determination of $C2/M1$.
2. Model uncertainties in the determination of $C2/M1$ due to the presence of non-resonant pion electro-production amplitudes that interfere with the extraction of the resonant amplitudes. These effects have been studied by employing theoretical pion electro-production models[33–37] in the data analysis (e.g. see Refs.[23–27]), and were experimentally investigated by measuring $C2/M1$ through an alternative reaction channel, the $p(e,e'p)\gamma$[27], were one employs a different theoretical framework for the ratio extraction.
3. The uncertainty of the symmetry breaking contributions δn_b.
4. In order to extract the G_E^n from the G_E^n/G_M^n ratio, we use a parametrization of the well known G_M^n, as typically done in such cases (e.g.[9,16] etc). Here we have used the one from Ref.[38]. The uncertainty introduced by G_M^n is studied by employing different G_M^n-parametrizations, and is found $\approx 0.5\%$, a small effect compared to the total uncertainty.

The relation between the G_E^n and the quadrupole transition form factors has also been established through large-N_c relations[22]. The relations take the form

$$\frac{E2}{M1}(Q^2) = \left(\frac{M_N}{M_\Delta}\right)^{3/2} \frac{M_\Delta^2 - M_N^2}{2Q^2} \frac{G_E^n(Q^2)}{F_2^p(Q^2) - F_2^n(Q^2)} \tag{2}$$

$$\frac{C2}{M1}(Q^2) = \left(\frac{M_N}{M_\Delta}\right)^{3/2} \frac{Q_+ Q_-}{2Q^2} \frac{G_E^n(Q^2)}{F_2^p(Q^2) - F_2^n(Q^2)} \tag{3}$$

where $F_2^{p(n)}$ are nucleon's Pauli form factors, M_Δ is the mass of the Δ, and $Q_\pm = ((M_\Delta \pm M_N)^2 + Q^2)^{\frac{1}{2}}$. Here one is free from any additional correction terms, such as the symmetry breaking contributions of Eq. 1. Another advantage is that the experimental data base is extended to include the Electric quadrupole (E2) transition, which in turn allows for an improved extraction of the G_E^n. Being able to extract the G_E^n independently through the Coulomb and the Electric quadrupole transitions offers a strong experimental test to the validity of the large-N_c relations and allows to quantify their level of theoretical uncertainty. The above relations come with a 15% theoretical uncertainty[22] that is treated accordingly in the G_E^n analysis. The G_E^n extraction from the Coulomb and from the Electric quadrupole transitions world data agree nicely within that level, as can be seen in Fig. 2, and validate this number. For the well known G_E^p, G_M^p and G_M^n that enter in the expressions through the Pauli form factors we use recent parametrizations; for the G_M^p and G_M^n we use[38], while for G_E^p we performed an updated parametrization so that we may include recent measurements from[39] that were not yet available in[38] using the widely used functional form

$$G_E^p = \frac{1 + (\sum\limits_{i=1}^{2} a_i x_i^i)}{(1 + \sum\limits_{j=1}^{4} b_j x_j^j)}. \tag{4}$$

In order to exhibit the potential of the method we have performed the G_E^n analysis with the JLab/Hall-A and MAMI/A1 measurements[23–27] at low-Q^2, in a kinematical region similar, and partially overlapping, to the proposed measurements. The results of the SU(6) based analysis and of the large-N_c analysis is in remarkable agreement as exhibited by the red and green points in Fig. 3(a). The weighted average of the two values leads to the final G_E^n result that is shown in Fig. 3(b) (blue circles), where the variance of the two values from the different analyses is assigned as an additional G_E^n theoretical uncertainty.

3 Neutron radius extraction

The neutron mean square charge radius is related to the slope of the neutron electric form factor as $Q^2 \to 0$ through

$$\langle r_n^2 \rangle = -6 \frac{dG_E^n(Q^2)}{dQ^2}\bigg|_{Q^2 \to 0}. \tag{5}$$

The $G_E^n(Q^2)$ has to be parametrized and fitted to the experimental data, and from the slope at $Q^2 = 0$ the $\langle r_n^2 \rangle$ is determined. Our studies, utilizing the low-Q^2 G_E^n data from the analysis of the JLab/Hall-A and MAMI/A1 measurements[23–27] as well as projected measurements from this proposal, have shown that the most robust function for the radius extraction takes the form

$$G_E^n(Q^2) = (1+Q^2/A)^{-2} \frac{B\tau}{1+C\tau}, \tag{6}$$

where $\tau = Q^2/4m_N^2$, and A, B, C are free parameters. It involves a similar form to the Galster[40]. The Galster is a long standing phenomenological parametrization that could adequately describe the early G_E^n data, but as recent experiments revealed it does not have sufficient freedom to accommodate reasonable values of the radius, without constraining or compromising the fit. Here, instead of using the standard dipole form factor with $\Lambda^2 = 0.71(GeV/c)^2$ an additional free parameter A is introduced (see Eq. 6). A second parametrization, giving a good fit to the data, involves the sum of two dipoles

$$G_E^n(Q^2) = \frac{A}{(1+\frac{Q^2}{B})^2} - \frac{A}{(1+\frac{Q^2}{C})^2}. \tag{7}$$

This form has been explored in the past[16] but with only two free parameters and with the $\langle r_n^2 \rangle$ already constrained by the measurement of the neutron-electron scattering length b_{ne}. Here we have removed the constraint on the neutron charge radius and we have introduced an additional free parameter. The fitted results of the two parametrizations come to an excellent agreement, with the two curves being nearly indistinguishable by eye, resulting to a nearly identical result for the r_n. Nevertheless, our studies revealed that the two-dipole fit suffers from limitations in the determination of the radius, and we will thus for consistency adopt only the paramterization of Eq. 6 for the extraction of $\langle r_n^2 \rangle$. The radius extraction will be repeated with multiple G_M^n parametrizations so that the uncertainty introduced by the G_M^n parametrization is quantified; our studies have shown that this uncertainty is approximately an order of magnitude smaller compared to the total $\langle r_n^2 \rangle$ uncertainty.

4 Flavor dependent form factors

The proposed G_E^n measurements will allow a unique insight into the flavor decomposition of the elastic nucleon electromagnetic form factors at low Q^2. To that end, one can follow the same line of work as previously done with the high Q^2 measurements[41]. Starting from the Dirac and Pauli nucleon form factors

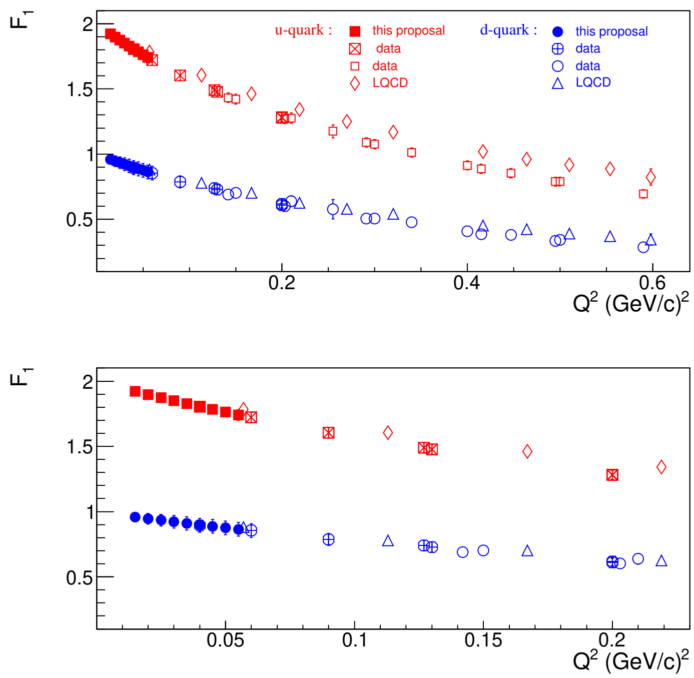

Figure 4. The projected measurements from the u- and d-quark flavor decomposition of the F_1 form factor. The F_1 form factor as derived for the neutron world data (empty-symbols) and from the G_E^n analysis of the[23–27] measurements (empty-crossed-symbols) is shown. The LQCD results that have been extracted using the data of[32] are also shown on the figure.

$F_1^{p(n)}$ and $F_2^{p(n)}$, under charge symmetry we perform the flavor decomposition of the form factors using the relations

$$F^u_{1(2)} = 2F^p_{1(2)} + F^n_{1(2)} \qquad F^d_{1(2)} = 2F^n_{1(2)} + F^p_{1(2)} \tag{8}$$

where with $F^u_{1(2)}$ and $F^d_{1(2)}$ we refer to the up and down quark contributions to the Dirac (Pauli) form factors of the proton. The normalizations of the Dirac form factors at $Q^2 = 0$ are given by $F_1^u(0) = 2$ and $F_1^d(0) = 1$ so as to yield a normalization of 2 and 1 for the u and the d-quark distributions in the proton, respectively. For the Pauli form factors at $Q^2 = 0$ the normalizations are given by $F_2^q(0) = \kappa_q$, where κ_u and κ_d can be expressed in terms of the proton (κ_p) and neutron (κ_n) anomalous magnetic moments as $\kappa_u \equiv 2\kappa_p + \kappa_n = +1.67$ and $\kappa_d \equiv \kappa_p + 2\kappa_n = -2.03$. The proposed measurements will extend the flavor decomposition of the form factors down to $Q^2 = 0.015\ (GeV/c)^2$, as seen in Fig. 4. Each data point corresponds to a G_E^n measurement, while for G_E^p, G_M^p and G_M^n a parametrization is utilized, as described earlier. The slopes of the flavor dependent Dirac form factors at $Q^2 = 0$ are related to the mean square radius of the quark distributions

$$\langle b^2_{u(d)} \rangle = \frac{-4}{F_1^{u(d)}(0)} \frac{dF_1^{u(d)}(Q^2)}{dQ^2}\bigg|_{Q^2 \to 0} \tag{9}$$

where b denotes the quark position in the plane transverse to the longitudinal momentum of a fast moving nucleon. Fitting the experimental $F_1^{u(d)}$ data we will extract these quantities with a high precision. This will in turn offer a direct measurement that will allow to cross check, and quantify, the indirect conclusion derived by the high-Q^2 measurements[41], where a wider distribution for the singly-represented quark, compared to the doubly-represented quarks, in the nucleon is suggested.

5 $N \to \Delta$ transition form factors

The first excited state of the nucleon dominates many nuclear phenomena at energies above the pion-production threshold and plays a prominent role in the physics of the strong interaction. The study of the transition form factors in-turn has allowed to explore various aspects of the nucleonic structure. Hadrons are composite systems with complex quark-gluon and meson cloud dynamics that give rise to non-spherical components in their wavefunction, which in a classical limit and at large wavelengths will correspond to a "deformation"[42–44]. The determination and subsequent understanding of the shapes of the fundamental building blocks in nature is a particularly fertile line of investigation for the understanding of the interactions of their constituents amongst themselves and the surrounding medium. For hadrons this means the interquark interaction and the quark-gluon dynamics. For the proton, the only stable hadron, the vanishing of the spectroscopic quadrupole moment, due to its spin 1/2 nature, precludes access to the most direct observable of deformation. As a result, the presence of the resonant quadrupole amplitudes $E_{1+}^{3/2}$ and $S_{1+}^{3/2}$ (or E2 and C2 photon absorption multipoles respectively) in the predominantly magnetic dipole $M_{1+}^{3/2}$ (or M1) $\gamma^* N \to \Delta$ transition has emerged as the experimental signature for such an effect[23–31,33,34,36,42–71]. Nonvanishing quadrupole amplitudes will signify that either the proton or the $\Delta^+(1232)$ or more likely both are characterized by non-spherical components in their wavefunctions. These amplitudes have been explored up to four momentum transfer squared $Q^2 = 7\ (GeV/c)^2$ [23–31,48–56,56–59,62–64] and the experimental results are in reasonable agreement with models invoking the presence of non-spherical components in the nucleon wavefunction.

In the constituent-quark picture of hadrons, the non-spherical amplitudes are a consequence of the non-central, color-hyperfine interaction among quarks[43,46]. However, it has been shown that this mechanism only provides a small fraction of the observed quadrupole signal at low momentum transfers, with the magnitudes of this effect for the predicted E2 and C2 amplitudes[47] being at least an order of magnitude too small to explain the experimental results and with the dominant M1 matrix element being $\approx 30\%$ low. A likely cause of these dynamical shortcomings is that such quark models do not respect chiral symmetry, whose spontaneous breaking leads to strong emission of virtual pions (Nambu-Goldstone Bosons)[45]. These couple to nucleons as $\vec{\sigma} \cdot \vec{p}$ where $\vec{\sigma}$ is the nucleon spin, and $\vec{p}$ is the pion momentum. The coupling is strong in the p wave and mixes in non-zero angular momentum components. Based on this, it is physically reasonable to expect that the pionic contributions increase the M1 and dominate the E2 and C2 transition matrix elements in the low Q^2 (large distance) domain. This was first indicated by adding pionic effects to quark models[65–67], subsequently in pion cloud model calculations[33,34], and recently demonstrated in Chiral Effective Field Theory calculations[68]. With the existence of these non-spherical amplitudes well established, recent high precision experiments and theoretical efforts have focused on testing in depth the reaction calculations and decoding the underlying nucleon dynamics. This proposal focuses on the low momentum transfer region, where the mesonic cloud dynamics is predicted to be dominant and rapidly changing (e.g. see Fig. 5), offering a test bed for chiral effective field theory calculations. Furthermore, the new measurements will be able to test the theoretical prediction that the Electric and the Coulomb quadrupole amplitudes converge as $Q^2 \to 0$.

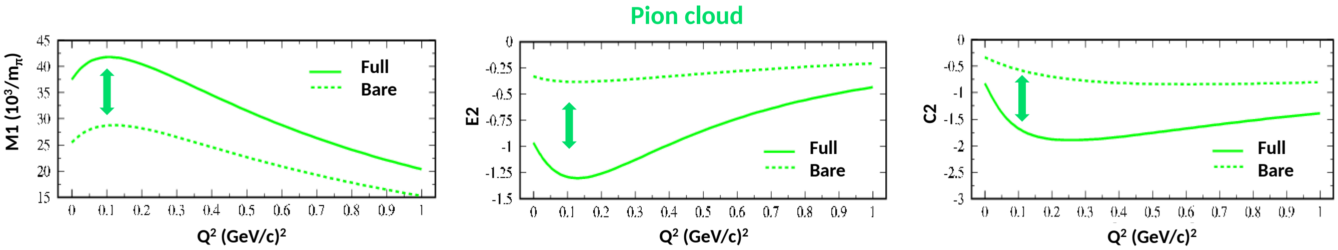

Figure 5. The effect of the pion cloud to the resonant amplitudes as predicted by the Sato Lee calculation (Bare: without the pion cloud).

6 The Experiment

6.1 Experimental apparatus and set-up

The experiment will involve measurements of the $p(e,e'p)\pi^0$ reaction. As shown in Fig. 6, the SHMS will detect the scattered electrons and the HMS will detect the protons. The undetected pion will be identified through the missing mass reconstruction. The spectrometers will employ their standard detector packages which are shown in Fig. 7 and Fig. 8 for the HMS and SHMS. For the SHMS, the Argon/Neon Cerenkov would be replaced by a vacuum pipe which is an additional standard SHMS detector stack configuration. This will reduce the multiple scattering before the SHMS drift chambers and improve the missing mass resolution. The target requested is a 4 cm LH2 cell, while the a beam current will be ranging from 6 μA to 15 μA. With the small expected π^- to electron rate (see Table 2) the calorimeter alone in the SHMS will provide all the needed π^- from electron separation. With the proton's momenta under 1.0 GeV/c, timing information will be more than sufficient to separate protons from π^+'s in the HMS. Dedicated optics runs will be required for the SHMS spectrometer since it will acquire data in momenta around 1 GeV/c, as well as a set of elastic runs for calibration and normalization purposes. The beam energy required is 1.3 GeV for all kinematic settings.

6.2 Kinematical Settings

The kinematical settings are summarized in Table 1. The SHMS spectrometer will be set to access a range of Q^2 settings, and for each one of these settings the HMS spectrometer will cover an extended phase space through a series of sequential measurements. The phase space that will be covered by the measurements is shown in Fig. 9, after the first layer of acceptance cuts and phase space masking has been applied. For the data analysis, the phase space will be further binned in nine Q^2 bins (increments of 0.005 $(GeV/c)^2$) and in 2 deg. bins in θ^*_{pq}. The beam current for the settings *b, c,* and *d* will be 15 μA. For the settings in group-*a* the beam current will be set to 6 μA so that the SHMS rate can stay below the 1 MHz level (recently, during the summer 2019 running period, we were able to operate the SHMS spectrometer at the 1.3 MHz rate without any concern, in a similar configuration during the E12-15-001 experiment). The HMS singles rate is at a comfortable level of a few tens of KHz for all the settings, as shown in Table 2. These rates have been calculated using the well established Wiser calculations for pions and protons, and the Bosted inelastic calculation folded with the SHMS acceptance for electron-singles. The signal-to-noise ratio (S/N), within a coincidence timing window of 1.5 ns, ranges between 1.2 and 7, as given in Table 1. Further suppression of accidentals can be achieved by applying a missing mass cut in the data analysis.

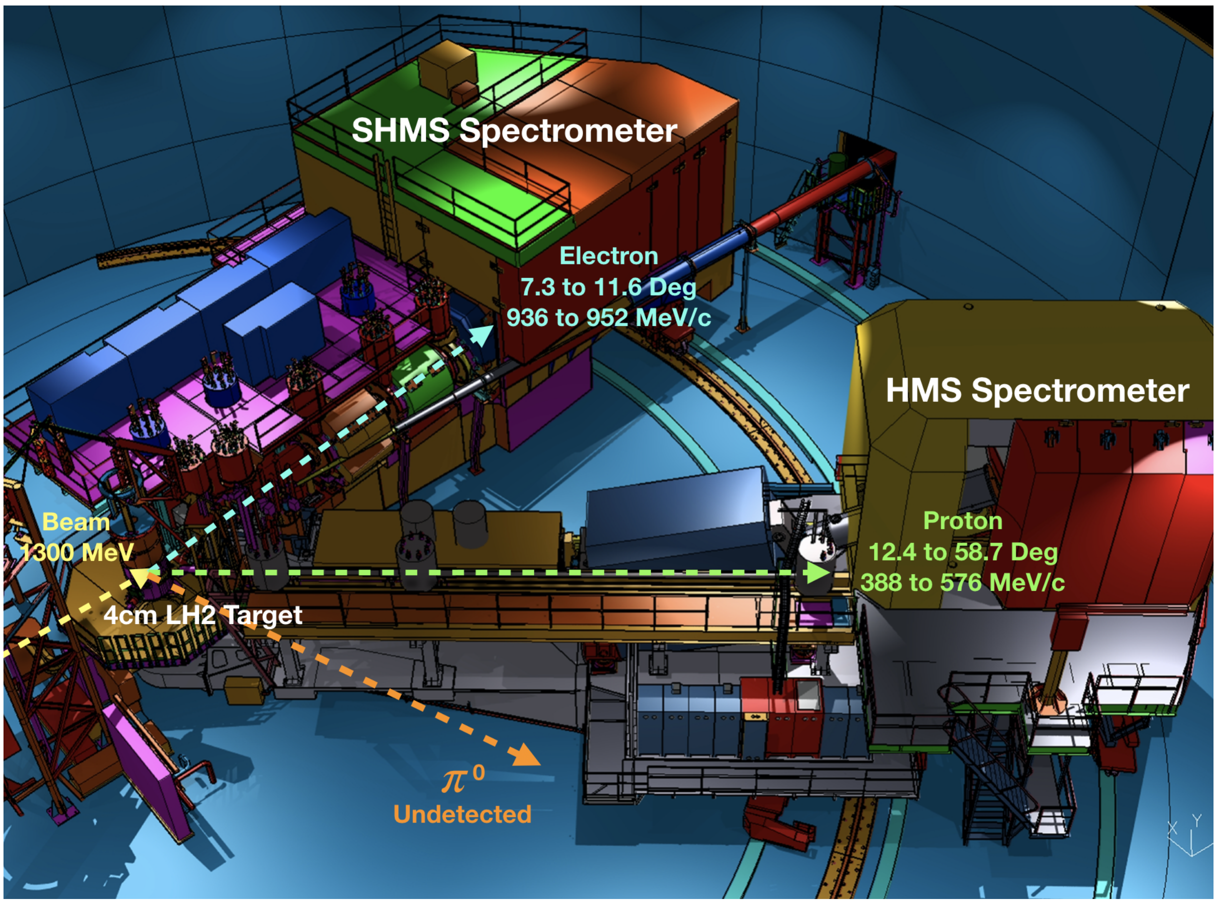

Figure 6. An illustration of the experimental hall and the proposed kinematic settings in Hall-C. See Tab. 1 for exact central angle and central momentum settings for each spectrometer arm.

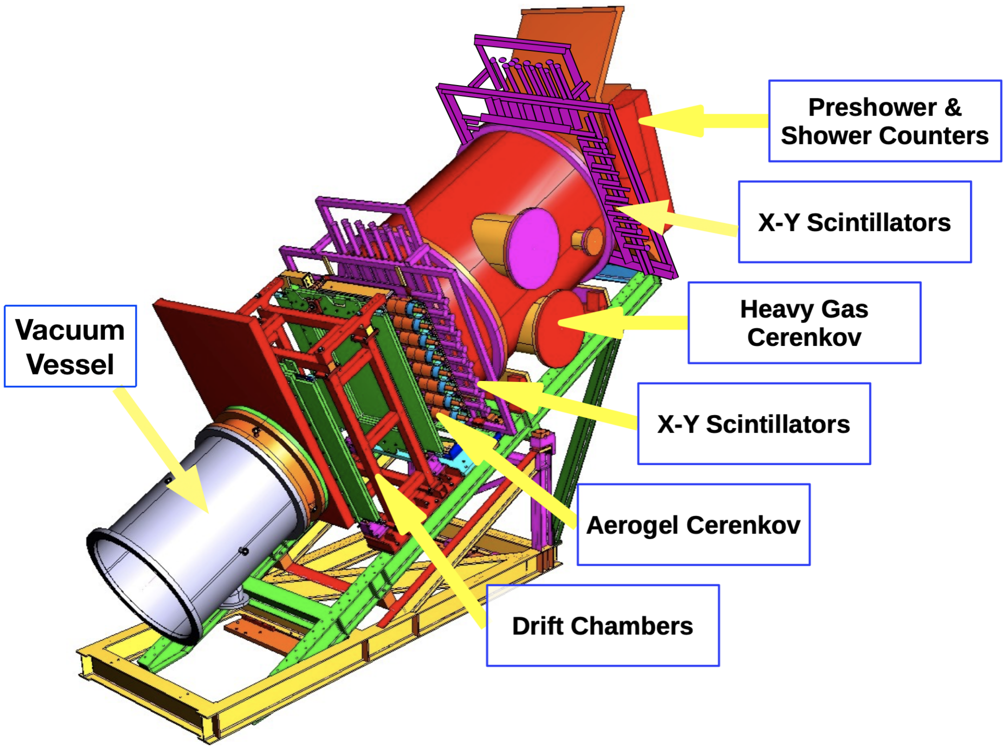

Figure 7. HMS Detector stack.

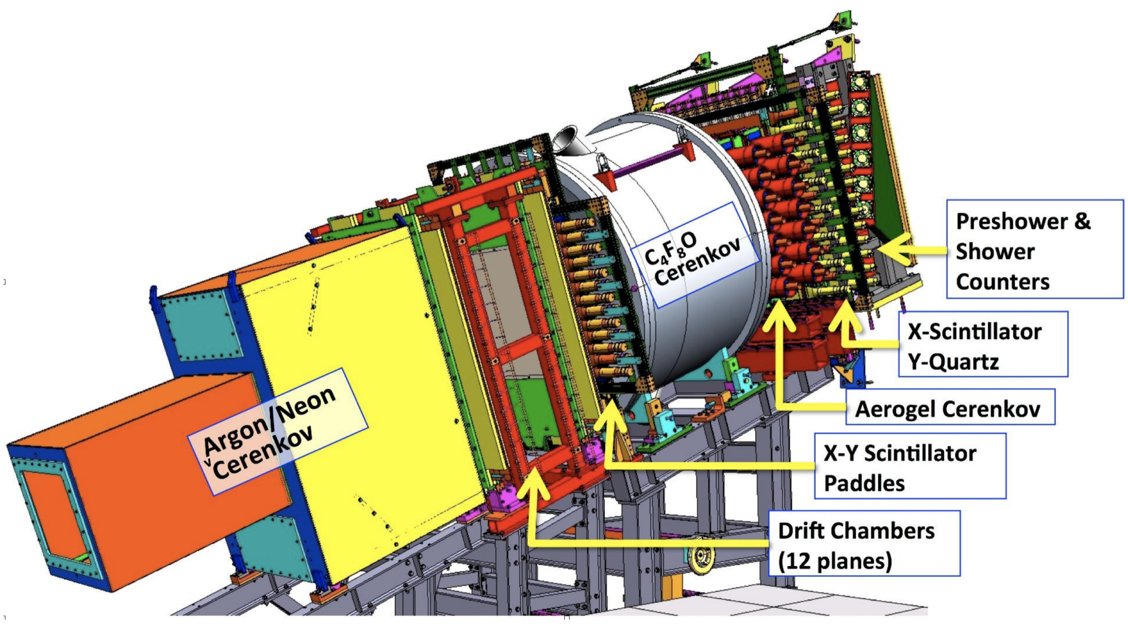

Figure 8. SHMS Detector stack. For this experiment, the standard SHMS configuration in which the Argon/Neon Cerenkov is replaced with a vacuum pipe will be used.

Setting	SHMS θ (deg)	SHMS P (MeV/c)	HMS θ (deg)	HMS P (MeV/c)	S/N	Time (hrs)
1a			18.77	532.53	2	7
2a			25.17	527.72	2	7
3a			33.7	506.61	3.2	6
4a	7.29	952.26	42.15	469.66	4.3	5
5a			50.44	418.56	4.9	5
6a			54.47	388.38	4.9	5
7a			12.37	527.72	2.7	6
1b			22.01	547.54	1.2	6
2b			28.24	542.61	1.4	6
3b			36.52	520.95	2.5	5
4b	8.95	946.93	44.64	483.08	3.4	4
5b			52.68	430.78	3.7	4
6b			56.53	399.92	3.5	4
7b			12.46	535.98	1.6	5
1c			24.40	562.00	1.5	9
2c			30.47	556.95	1.9	9
3c			38.52	534.79	3.5	6
4c	10.37	941.61	46.47	496.06	4.4	6
5c			54.17	442.64	4.8	6
6c			57.85	411.16	4.8	6
7c			12.69	543.24	2	6
1d			26.24	575.96	1.8	12
2d			32.16	570.80	2.5	11
3d			40.01	548.17	4.5	8
4d	11.63	936.28	47.73	508.64	5.5	8
5d			55.18	454.17	6.9	7
6d			58.71	422.13	6	8
7d			12.47	548.17	2.1	10

Table 1. The kinematical settings of the proposed measurements. The signal-to-noise ratio and the required beam time are given for each setting.

Setting	SHMS e^- (KHz)	SHMS π^-(KHz)	HMS p (KHz)	HMS π^+ (KHz)
1a	970.2	5.04	5.1	25.6
2a			5.6	23.5
3a			5.3	19.1
4a			4.3	15.9
5a			3.2	14.8
6a			2.6	15.1
7a			4.0	23.8
1b	885.1	11.5	11.6	49.7
2b			11.8	42.7
3b			10.4	33.3
4b			8.2	27.7
5b			5.8	26.2
6b			4.7	27.3
7b			8.4	49.3
1c	510.0	12.0	11.9	45.3
2c			11.6	37.3
3c			9.8	28.4
4c			7.5	23.5
5c			5.2	22.9
6c			4.1	24.2
7c			8.6	49.1
1d	331.1	12.3	11.9	40.9
2d			11.2	32.8
3d			9.2	24.6
4d			6.9	20.5
5d			4.7	20.3
6d			3.6	21.7
7d			8.6	48.7

Table 2. Singles rates for the SHMS and the HMS spectrometers.

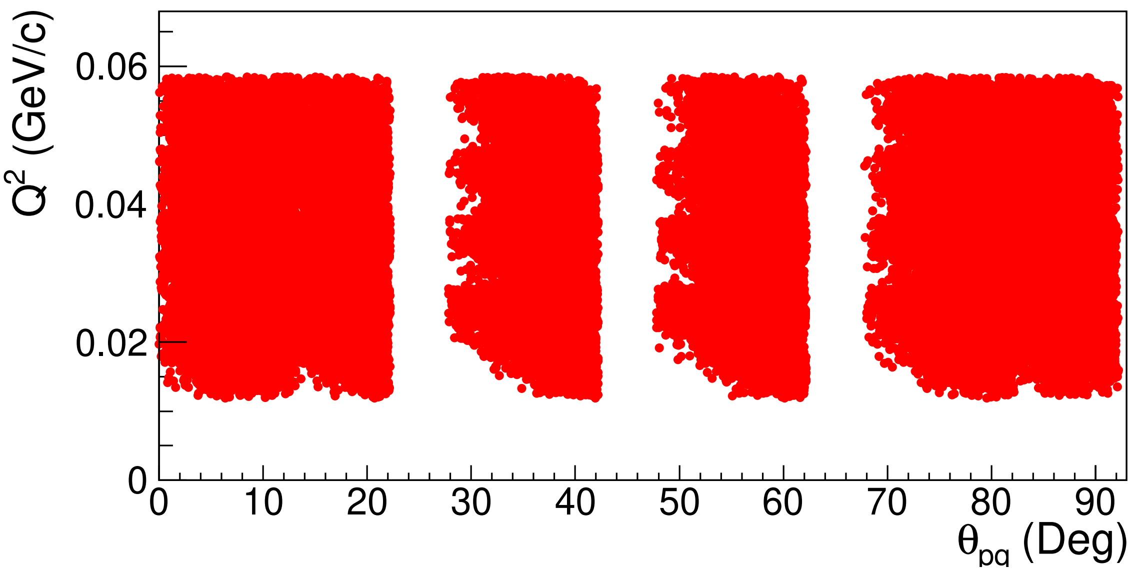

Figure 9. The phase space that will be accessed by the proposed measurements, after a first layer of acceptance cuts and phase space masking has been applied.

6.3 Data analysis and projected results

The cross section of the $p(e,e'p)\pi^\circ$ reaction is sensitive to a set of independent partial responses $(\sigma_T, \sigma_L, \sigma_{LT}, \sigma_{TT})$:

$$\frac{d^5\sigma}{d\omega d\Omega_e d\Omega_{pq}^{cm}} = \Gamma(\sigma_T + \varepsilon\cdot\sigma_L - v_{LT}\cdot\sigma_{LT}\cdot\cos\phi_{pq}^* + \varepsilon\cdot\sigma_{TT}\cdot\cos 2\phi_{pq}^*)$$

where $v_{LT} = \sqrt{2\varepsilon(1+\varepsilon)}$ is a kinematic factor, ε is the transverse polarization of the virtual photon, Γ is the virtual photon flux, and ϕ_{pq}^* is the proton azimuthal angle with respect to the electron scattering plane. The differential cross sections ($\sigma_T, \sigma_L, \sigma_{LT}, \sigma_{TT}$, and $\sigma_{LT'}$) are all functions of the center-of-mass energy W, the Q^2, and the proton center of mass polar angle θ_{pq}^* (measured from the momentum transfer direction). The $\sigma_0 = \sigma_T + \varepsilon \cdot \sigma_L$ response is dominated by the M_{1+} resonant multipole while the interference of the $C2$ and $E2$ amplitudes with the $M1$ dominates the Longitudinal - Transverse and Transverse - Transverse responses, respectively. Cross section measurements will be performed on the nucleon resonance region, extending from $Q^2 = 0.015\ (GeV/c)^2$ to $Q^2 = 0.055\ (GeV/c)^2$ and covering the θ_{pq}^* range from 0° to 90°. For part of the θ_{pq}^* coverage (due to space limiataions of the experimental setup) the proton spectrometer will be sequentially placed at $\phi_{pq}^* = 0^\circ$ and 180°, thus allowing to measure the in-plane azimuthal asymmetry of the cross section with respect to the momentum transfer direction, $A_{(\phi_{pq}=0,\pi)} = [\sigma_{\phi_{pq}=0} - \sigma_{\phi_{pq}=180}]/[\sigma_{\phi_{pq}=0} + \sigma_{\phi_{pq}=180}]$, which will enhance the sensitivity to the measurement of the Coulomb quadrupole amplitude. Here, for the pair of $\phi_{pq}^* = 0^\circ$ and 180° measurements the cross sections and asymmetries will be obtained with the phase space matched in (W,Q^2,θ_{pq}^*). A first level of acceptance cuts will be applied in the data analysis in order to limit the phase space to the central region of the spectrometers and to ensure that potential edge effects will be avoided, and after that the phase space will be further binned. Point cross sections will be extracted from the finite acceptances by utilizing the cross section calculations from the state of the art theoretical models[33–37] in the Monte Carlo simulation, while radiative corrections will also be applied to the data analysis using the Monte

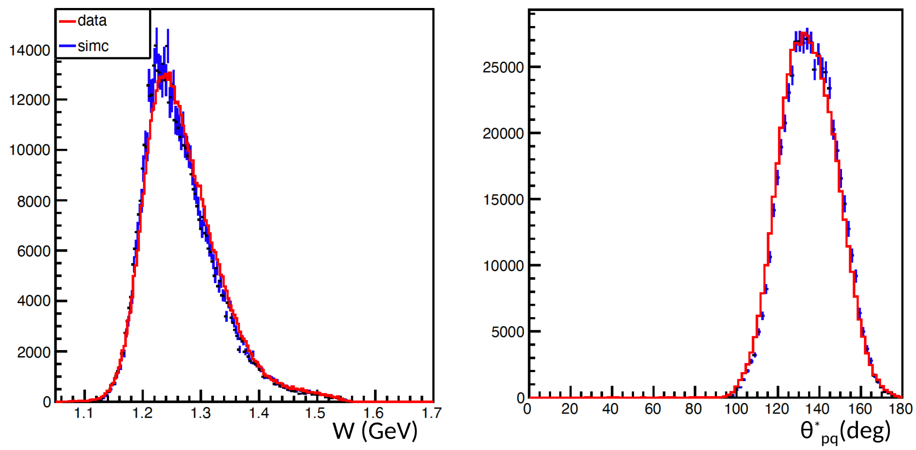

Figure 10. The parasitic measurement of the $p(e,e'p)\pi^\circ$ reaction at $Q^2 = 0.3~(GeV/c)^2$ during the E12-15-001 data taking, using the same experimental arrangement that will be used in the proposed measurements. The simulation has been weighted with the MAID cross section.

Carlo simulation. The cross section systematic uncertainties will be of the order of 3%, dominating over the better than 1% statistical uncertainties. The systematic uncertainties are driven by the level of understanding of the acceptance, the uncertainty of the beam energy and of the scattering angle, and to a smaller extent by the target density, detector efficiencies, target cell background, target length, beam charge, dead time corrections (each contributing in the range of 0.5% to 0.3%). In the asymmetry measurements the systematic uncertainties will be further suppressed through the cross section ratio, while an advantage is presented here by the fact that the electron spectrometer position and momentum settings do not change during the asymmetry measurements. This level of uncertainties has been successfully demonstrated in similar measurements that we have performed in the past, at JLab and at MAMI, with similar experimental setups e.g. [23–26] and at a similar Q^2 range. Furthermore, we recently had the opportunity to measure the same reaction channel, through a parasitic measurement, during the running of the E12-15-001 experiment. This measurement was performed at a slightly higher momentum transfer, at $Q^2 = 0.3~(GeV/c)^2$, but with the exact same experimental setup that we propose here i.e. with the SHMS and the HMS spectrometers detecting electrons and protons in coincidence, respectively. The preliminary analysis of this data has demonstrated an excellent understanding of the coincidence acceptance and of the systematic uncertainties, as well as the readiness of all the experimental and theoretical tools involved in this effort. In Fig. 10 the comparison of the data with the simulation is presented. The simulation has been weighted with the MAID cross section, which has been tested to be very successful in this kinematical region. The data have been corrected for all known efficiencies (and they have not been arbitrarily normalized to the simulation). The comparison illustrates the excellent understanding of the acceptance within the simulation, as well as the excellent measurement of the reaction's cross section.

An important aspect of these measurements involves the treatment of the non-resonant pion electroproduction amplitudes that interfere with the extraction of the resonant amplitudes in the $N \to \Delta$ transition. These interfering contributions, small in magnitude but large in number, can not be sufficiently constrained by the experimental measurements, and they thus result into a model uncertainty for the quadrupole transition form factors. In the past these contributions have been frequently poorly studied or quoted as an uncertainty. Here, the effect of these amplitudes has been studied in the following manner. State of the art theoretical pion electroproduction models[33–37] will be employed in the data analysis. Fits of the resonant amplitudes will be performed while taking into account the contributions of background amplitudes from

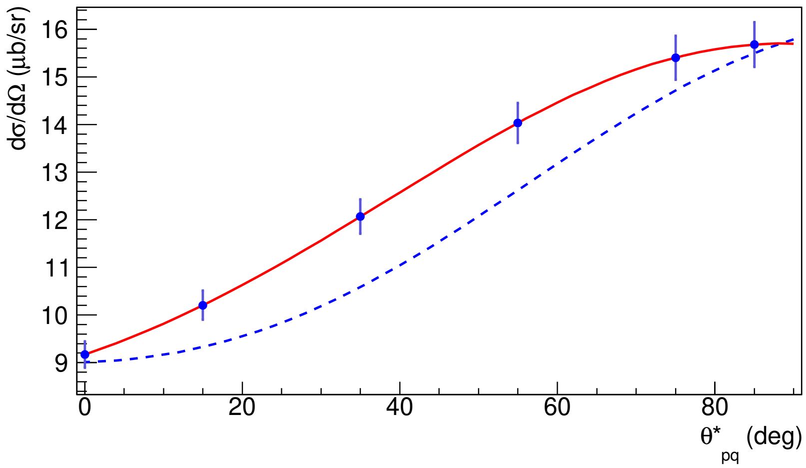

Figure 11. Projected cross section measurements at $Q^2 = 0.02\ (GeV/c)^2$ and $\phi^*_{pq} = 180°$. The solid line shows the MAID cross section (C2/M1=-4.5%). The dashed line shows the cross section prediction for C2=0.

the different models. The models offer different descriptions for the background amplitudes, leading to deviations in the extracted values of the transition form factors that are quantified as a model uncertainty. This uncertainty will in-turn be appropriately treated in the extraction of the G^n_E. This procedure has been previously applied in earlier measurements that our group has performed at JLab and at MAMI e.g.[23–26]. The validity of the model uncertainties can be experimentally tested when one studies the excitation through the weak $p(e,e'p)\gamma$ channel. In this case the same physics signal can be extracted within a different theoretical framework, thus offering an ideal cross-check to the model uncertainties associated with the pion electroproduction channel. The branching ratio of the photon channel is very small (0.6%), two orders of magnitude smaller compared to the pion-electroproduction, and as such it was not studied until recently. To that end, the first such measurement was conducted at MAMI (A1)[27]. Measurements were performed at the same Q^2 and utilizing the same experimental setup, as in the measurement of the pion channel. The results were found in very good agreement between the two channels[26,27], thus giving credence to the quantification of the model uncertainties with the above procedure.

The two quadrupole transition amplitudes will be measured with a 20% to 25% uncertainty, depending on the kinematics, while the dominant magnetic dipole amplitude will be measured to a few % level. The projected measurements for the two quadrupole amplitudes are shown in Fig. 12. The G^n_E will then be extracted from the quadrupole amplitudes, following the procedure described in the earlier section. The variance of the extracted values from the large-N_c and from the SU(6) data analysis will be assigned as a theoretical uncertainty for G^n_E. This uncertainty is typically a factor of 2 smaller compared to the experimental uncertainty, as can be seen e.g. in Fig. 3(a), and is not a dominant factor in the neutron charge radius extraction. The projected G^n_E measurements are shown in Fig. 14. The $\langle r^2_n \rangle$ will be derived through Eq. 5 by fitting the parametrization of Eq. 6, as described in the radius extraction section. The measurements will allow to extract the $\langle r^2_n \rangle$ with an uncertainty of $\pm 0.005\ (fm^2)$, as shown in Fig. 13, thus offering a measurement of equivalent precision to the radius extraction that is based on the measurement of the neutron-electron scattering length. From the G^n_E measurements we will perform the flavor decomposition of the nucleon form factors, as described earlier in the flavor-dependent form factors section; the projected measurements are shown in Fig. 4. From the $F_1^{u(d)}$ data, the mean square radius of

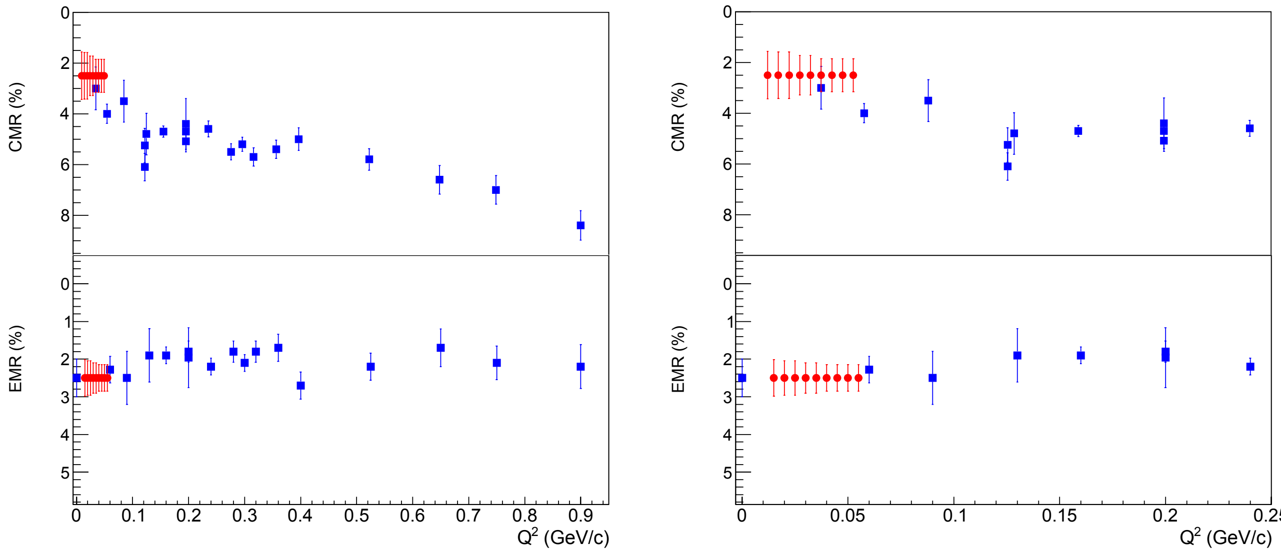

Figure 12. The projected CMR and EMR measurements (red) and the world data (blue).

the quark distributions $\langle b^2_{u(d)} \rangle$ will be determined through Eq. 9. A variety of functional forms will be employed in the fits, so that all functions that can provide a good fit are considered, and the variance of the fitted results is accounted for in the uncertainty. The projected measurements will allow to determine the $\langle b^2_{u(d)} \rangle$ at the percent level.

7 Summary

In this Letter of Intent we propose to measure the neutron charge radius. The neutron, along with it's isospin partner the proton, are cornerstones in our depiction of the visible universe, since they together comprise more than 99% of it's matter. A precise determination of the nucleon's size is unquestionably an essential piece in our understanding of the nucleon's structure. The neutron has proved to be a very challenging system to study in the lab. Contrary to the proton, there is no equivalent atomic method possible for the measurement of its radius, and the electron scattering method suffers from limitations due to the absence of a free neutron target. As a result, the determination of the neutron charge radius, r_n, has in the past relied solely on one method, the measurement of the *neutron*-electron scattering length. The most recent measurements date back to the end of the previous century[3], while the PDG adopted results exhibit discrepancies that remain unresolved to this day[3],[5].

Here, we propose to measure the neutron's charge radius using a new approach: by determining the G^n_E slope at $Q^2 \to 0$, taking advantage of the long known connection between the quadrupole transition form factors of the proton and the neutron electric form factor, which comes as a result of the fundamental symmetry of the two systems. Following that path, we can overcome the limitations of previous methods and access otherwise inaccessible low momentum transfers, thus making a precise r_n extraction possible. The connection between the quadrupole amplitudes and the neutron electric form factor comes with a theoretical uncertainty at the 10% to 15% level which is accounted for in the radius extraction. That level of uncertainty is well justified on very strong theoretical foundations, but can be further supported also by experimental data. Furthermore, it is not a limiting factor in these measurements since the experimental

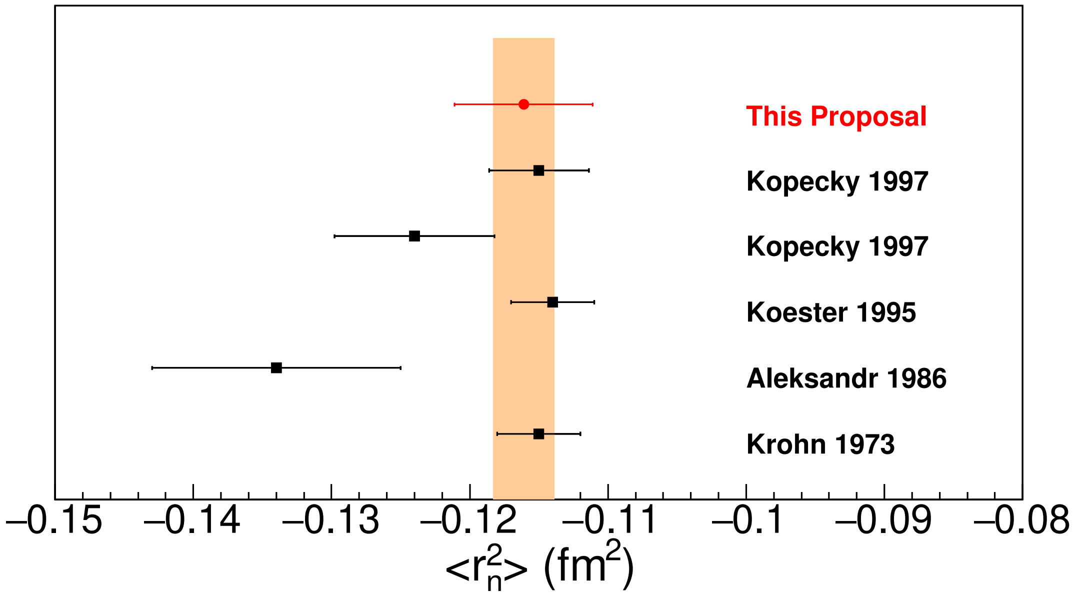

Figure 13. The proposed $\langle r_n^2 \rangle$ measurement is shown (red point) projected on the PDG value. The measurements from the references[3–6] that are included in the PDG analysis for the $\langle r_n^2 \rangle$ are also shown. The band marks the PDG averaged $\langle r_n^2 \rangle$ value.

uncertainties overtake the level of theoretical uncertainties. The proposed measurements carry significant scientific merit for a number of reasons. First, it offers valuable input towards addressing the long standing unresolved discrepancies of the r_n measurements. Secondly, it opens a new path for further improvement of the r_n extraction. Thirdly, for the first time an alternative method is presented for the measurement of this fundamental quantity; alternative methods have proven most valuable in the case of the proton where the disagreement of the charge radius, r_p, as determined using different experimental approaches[1] gave rise to the proton radius puzzle[2] and led to a significant effort in[39,72–74]. Considering the fundamental symmetry between the neutron and the proton systems, it becomes important to extensively study the neutron charge radius by exploring alternative methods, for the exact same nature of reasons.

The experiment will require standard Hall C equipment, namely a 4 cm liquid hydrogen target, an 1.3 GeV beam with $I = 15\ \mu A$, and the SHMS and the HMS spectrometers with their standard detector packages, for the measurement of electrons and protons, respectively. The experiment will need to acquire data for 7.8 days at full efficiency, and an additional day for optics and normalization measurements, so that the $\langle r_n^2 \rangle$ can be determined within $\pm 0.005\ (fm)^2$.

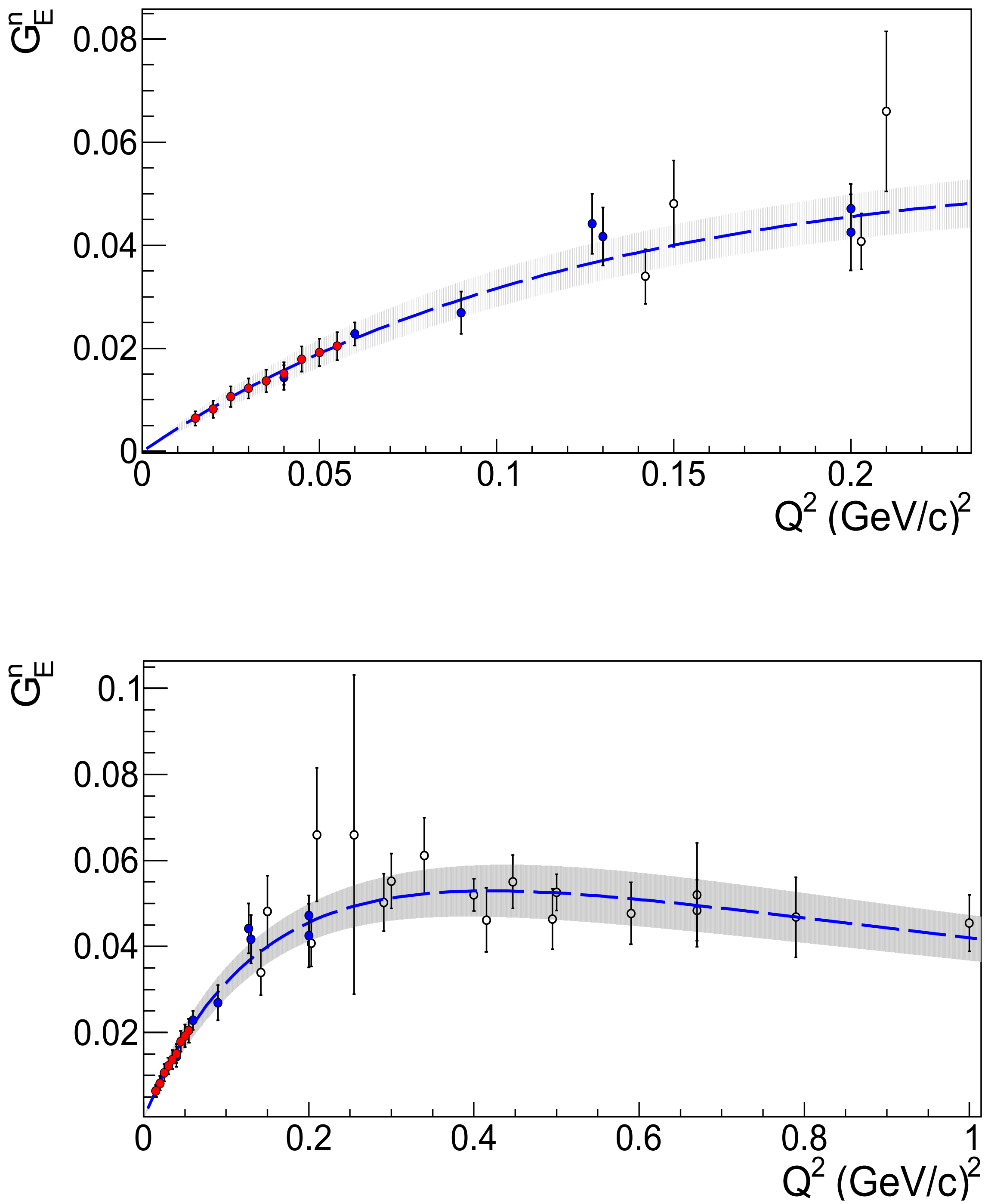

Figure 14. The projected G_E^n measurements (shown in red). The G_E^n world data are also shown (white) along with the G_E^n analysis of the measurements[23–27] (blue). The top panel shows a zoomed-in perspective of the low-Q^2 region.

References

1. Pohl, R. *et al.* The size of the proton. *Nature* **466**, 213–216 (2010).
2. R. Pohl, G. A. M., R. Gilman & Pachucki, K. Muonic hydrogen and the proton radius puzzle. *Ann. Rev. Nucl. Part. Sci.* **63**, 175–204 (2013).
3. Kopecky, S. *et al.* Neutron charge radius determined from the energy dependence of the neutron transmission of liquid Pb-208 and Bi-209. *Phys. Rev.* **C56**, 2229–2237 (1997).
4. Koester, L. *et al.* Neutrino electron scattering length and electric polarizability of the neutron derived from cross-sections of bismuth and of lead and its isotopes. *Phys. Rev.* **C51**, 3363–3371 (1995).
5. Aleksandrov, Yu. A., Vrana, M., Manrique, G. J., Machekhina, T. A. & Sedlakova, L. N. Neutron rms radius and electric polarizability from data on the interaction of slow neutrons with bismuth. *Sov. J. Nucl. Phys.* **44**, 900–902 (1986).
6. Krohn, V. E. & Ringo, G. R. Reconsiderations of the electron - neutron scattering length as measured by the scattering of thermal neutrons by noble gases. *Phys. Rev.* **D8**, 1305–1307 (1973).
7. Madey, R. *et al.* Measurements of G_E^n/G_M^n from the $^2H(\vec{e},e'\vec{n})^1H$ reaction to $Q^2 = 1.45\ (GeV/c)^2$. *Phys. Rev. Lett.* **91**, 122002 (2003).
8. Schlimme, B. S. *et al.* Measurement of the neutron electric to magnetic form factor ratio at $Q^2 = 1.58$ GeV^2 using the reaction $^3\vec{H}e(\vec{e},e'n)pp$. *Phys. Rev. Lett.* **111**, 132504 (2013).
9. Riordan, S. *et al.* Measurements of the Electric Form Factor of the Neutron up to Q^2=3.4 GeV^2 using the Reaction $^3\vec{H}e(\vec{e},e'n)pp$. *Phys. Rev. Lett.* **105**, 262302 (2010).
10. Glazier, D. I. *et al.* Measurement of the electric form-factor of the neutron at $Q^2 = 0.3\ (GeV/c)^2$ to $0.8\ (GeV/c)^2$. *Eur. Phys. J.* **A24**, 101–109 (2005).
11. Plaster, B. *et al.* Measurements of the neutron electric to magnetic form-factor ratio G_{En}/G_{Mn} via the $^2H(\vec{e},e',\vec{n})^1H$ reaction to Q^2 =1.45 $(GeV/c)^2$. *Phys. Rev.* **C73**, 025205 (2006).
12. Zhu, H. *et al.* A Measurement of the electric form-factor of the neutron through $\vec{d}(\vec{e},e'n)p$ at $Q^2 = 0.5$ $(GeV/c)^2$. *Phys. Rev. Lett.* **87**, 081801 (2001).
13. Warren, G. *et al.* Measurement of the electric form-factor of the neutron at $Q^2 = 0.5$ and 1.0 GeV^2/c^2. *Phys. Rev. Lett.* **92**, 042301 (2004).
14. Rohe, D. *et al.* Measurement of the neutron electric form-factor $G_{(en)}$ at $0.67(GeV/c)^2$ via $^3\vec{H}e(\vec{e},e'n)$. *Phys. Rev. Lett.* **83**, 4257–4260 (1999).
15. Bermuth, J. *et al.* The Neutron charge form-factor and target analyzing powers from $^3\vec{H}e(\vec{e},e'n)$ scattering. *Phys. Lett.* **B564**, 199–204 (2003).
16. Geis, E. *et al.* The Charge Form Factor of the Neutron at Low Momentum Transfer from the $^2\vec{H}(\vec{e},e'n)p$ Reaction. *Phys. Rev. Lett.* **101**, 042501 (2008).
17. Eden, T. *et al.* Electric form factor of the neutron from the $^2\vec{H}(\vec{e}$,e'n$)^1H$ reaction at Q^2=0.255 $(GeV/c)^2$. *Phys. Rev. C* **50**, R1749–R1753 (1994).
18. Ostrick, M. *et al.* Measurement of the Neutron Electric Form Factor $G_{E,n}$ in the Quasifree $^2H(\vec{e},e'\vec{n})p$ Reaction. *Phys. Rev. Lett.* **83**, 276–279 (1999).

19. Golak, J., Ziemer, G., Kamada, H., Witała, H. & Glöckle, W. Extraction of electromagnetic neutron form factors through inclusive and exclusive polarized electron scattering on a polarized ^{3}He target. *Phys. Rev. C* **63**, 034006 (2001).

20. Herberg, C. *et al.* Determination of the neutron electric form-factor in the D(e,e' n)p reaction and the influence of nuclear binding. *Eur. Phys. J.* **A5**, 131–135 (1999).

21. Buchmann, A. J. Electromagnetic N —> Δ transition and neutron form-factors. *Phys. Rev. Lett.* **93**, 212301 (2004).

22. Pascalutsa, V. & Vanderhaeghen, M. Large-N_c relations for the electromagnetic nucleon-to-Δ form factors. *Phys. Rev.* **D76**, 111501(R) (2007).

23. Blomberg, A. *et al.* Electroexcitation of the $\Delta^+(1232)$ at low momentum transfer. *Phys. Lett.* **B760**, 267–272 (2016).

24. Stave, S. *et al.* Lowest Q^2 Measurement of the $\gamma *$ p —> Δ Reaction: Probing the Pionic Contribution. *Eur. Phys. J.* **A30**, 471–476 (2006).

25. Sparveris, N. *et al.* Measurements of the γ*p $\rightarrow$ Δ reaction at low Q^2. *Eur. Phys. J.* **A49**, 136 (2013).

26. Sparveris, N. F. *et al.* Determination of quadrupole strengths in the $\gamma * p \rightarrow \Delta(1232)$ transition at Q^2 = 0.20 $(GeV/c)^2$. *Phys. Lett.* **B651**, 102–107 (2007).

27. Blomberg, A. *et al.* Virtual Compton Scattering measurements in the nucleon resonance region. *Eur. Phys. J. A* **55**, 182 (2019). 1901.08951.

28. Sparveris, N. F. *et al.* Investigation of the conjectured nucleon deformation at low momentum transfer. *Phys. Rev. Lett.* **94**, 022003 (2005).

29. Elsner, D. *et al.* Measurement of the LT-asymmetry in π^0 electroproduction at the energy of the $\Delta(1232)$ resonance. *Eur. Phys. J.* **A27**, 91–97 (2006).

30. Aznauryan, I. G. *et al.* Electroexcitation of nucleon resonances from CLAS data on single pion electroproduction. *Phys. Rev.* **C80**, 055203 (2009).

31. Kelly, J. J. *et al.* Recoil polarization measurements for neutral pion electroproduction at Q^2 = 1 $(GeV/c)^2$ near the Delta resonance. *Phys. Rev.* **C75**, 025201 (2007).

32. Alexandrou, C. *et al.* Proton and neutron electromagnetic form factors from lattice QCD. *Phys. Rev.* **D100**, 014509 (2019).

33. Kamalov, S. & Yang, S. N. Pion cloud and the Q^2 dependence of $\gamma *$ N <—> Δ transition form-factors. *Phys. Rev. Lett.* **83**, 4494–4497 (1999).

34. Sato, T. & Lee, T. Dynamical study of the Delta excitation in N (e, e-prime pi) reactions. *Phys. Rev. C* **63**, 055201 (2001).

35. Drechsel, D., Hanstein, O., Kamalov, S. S. & Tiator, L. A Unitary isobar model for pion photoproduction and electroproduction on the proton up to 1-GeV. *Nucl. Phys.* **A645**, 145–174 (1999).

36. Kamalov, S., Chen, G.-Y., Yang, S.-N., Drechsel, D. & Tiator, L. Pi0 photoproduction and electroproduction at threshold within a dynamical model. *Phys. Lett. B* **522**, 27–36 (2001).

37. Arndt, R. A., Briscoe, W. J., Strakovsky, I. I. & Workman, R. L. Analysis of pion photoproduction data. *Phys. Rev.* **C66**, 055213 (2002).

38. Ye, Z., Arrington, J., Hill, R. J. & Lee, G. Proton and Neutron Electromagnetic Form Factors and Uncertainties. *Phys. Lett.* **B777**, 8–15 (2018).

39. Xiong, W. *et al.* A small proton charge radius from an electron–proton scattering experiment. *Nature* **575**, 147–150 (2019).

40. Galster, S. *et al.* Elastic electron-deuteron scattering and the electric neutron form factor at four-momentum transfers $5\text{fm}^{-2} < q^2 < 14\text{fm}^{-2}$. *Nucl. Phys. B* **32**, 221–237 (1971).

41. Cates, G. D., de Jager, C. W., Riordan, S. & Wojtsekhowski, B. Flavor decomposition of the elastic nucleon electromagnetic form factors. *Phys. Rev. Lett.* **106**, 252003 (2011).

42. A. de Rujula, H. G. & Glashow, S. *Phys. Rev. D* **12**, 147 (1975).

43. Glashow, S. *Physica* **96A**, 27 (1979).

44. Bernstein, A. & Papanicolas, C. Shapes of hadrons. *AIP. Conf. Proc.* **904**, 1 (2007).

45. Bernstein, A. *Eur. Phys. J. A* **17**, 349 (2003).

46. N. Isgur, G. K. & Koniuk, R. *Phys. Rev.* **D25**, 2394 (1982).

47. Capstick, S. & Karl, G. *Phys. Rev.* **D41**, 2767 (1990).

48. Blanpied, G. *Phys. Rev. Lett.* **79**, 4337 (1997).

49. et al., R. B. *Phys. Rev. Lett.* **78**, 606 (1997).

50. et al., R. B. *Phys. Rev.* **C61**, 035204 (2000).

51. et al., V. F. *Phys. Rev. Lett.* **82**, 45 (1999).

52. et al., T. P. *Phys. Rev. Lett.* **86**, 2959 (2001).

53. et al., C. M. *Phys. Rev. Lett.* **86**, 2963 (2001).

54. et al., P. B. *Phys. Rev. Lett.* **88**, 142001 (2002).

55. van Buuren et al., L. *Phys. Rev. Lett.* **89**, 012001 (2002).

56. van Buuren et al., L. *Phys. Rev. C* **70**, 042201 (2004).

57. et al., C. K. *Phys. Lett. B.* **564**, 21 (2003).

58. Kelly, J. *Phys. Rev. Lett.* **95**, 102001 (2005).

59. et al., M. U. *Phys. Rev. Lett.* **97**, 112003 (2006).

60. et al., C. A. *Phys. Rev. Lett.* **94**, 021601 (2005).

61. SAID. http://gwdac.phys.gwu.edu.

62. et al., S. S. *Phys. Rev. C* **78**, 024209 (2008).

63. et al., A. N. V. *Phys. Rev. C* **80**, 035203 (2009).

64. van Buuren et al., L. *Phys. Rev. C* **84**, 028201 (2011).

65. D.-H. Lu, A. W. T. & Williams, A. G. *Phys. Rev. C* **55**, 3108 (1997).

66. U. Meyer, E. H. & Buchmann, A. J. *Phys. Rev. C* **64**, 035203 (2001).

67. M. Fiolhais, B. G. & Sirca, S. *Phys. Lett. B* **373**, 229 (1996).

68. Pascalutsa, V. & Vanderhaeghen, M. *Phys. Rev. D* **73**, 034003 (2006).

69. Gail, T. A. & Hemmert, T. R. *Eur. Phys. J A* **28**, 91 (2006).

70. et al., M. D. S. *Nucl. Phys. A* **755**, 294 (2005).

71. et al., J. M. *Phys. Rev. Lett.* **72**, 3325 (1994).

72. Antognini, A. *et al.* Proton Structure from the Measurement of 2S-2P Transition Frequencies of Muonic Hydrogen. *Science* **339**, 417 (2013).

73. Flaurbaey, H. *et al.* New measurement of the 1S–3S transition frequency of hydrogen: contribution to the proton charge radius puzzle. *Phys. Rev. Lett.* **120**, 182001 (2018).

74. Bezginov, N. *et al.* A measurement of the atomic hydrogen Lamb shift and the proton charge radius. *Science* **365**, 1007 (2019).